Time-Periodic Electro-Osmotic Flow With Nonuniform Surface Charges

Hyunsung Kim
School of Mechanical and Materials Engineering,
Washington State University,
Pullman, WA 99164-2920
e-mail: hyunsung.kim@wsu.edu

Aminul Islam Khan
School of Mechanical and Materials Engineering,
Washington State University,
Pullman, WA 99164-2920
e-mail: aminulislam.khan@wsu.edu

Prashanta Dutta[1]
School of Mechanical and Materials Engineering,
Washington State University,
Pullman, WA 99164-2920
e-mail: prashanta@wsu.edu

Mixing in a microfluidic device is a major challenge due to creeping flow, which is a significant roadblock for development of lab-on-a-chip device. In this study, an analytical model is presented to study the fluid flow behavior in a microfluidic mixer using time-periodic electro-osmotic flow. To facilitate mixing through microvortices, nonuniform surface charge condition is considered. A generalized analytical solution is obtained for the time-periodic electro-osmotic flow using a stream function technique. The electro-osmotic body force term is accounted as a slip boundary condition on the channel wall, which is a function of time and space. To demonstrate the applicability of the analytical model, two different surface conditions are considered: sinusoidal and step change in zeta potential along the channel surface. Depending on the zeta potential distribution, we obtained diverse flow patterns and vortices. The flow circulation and its structures depend on channel size, charge distribution, and the applied electric field frequency. Our results indicate that the sinusoidal zeta potential distribution provides elliptical shaped vortices, whereas the step change zeta potential provides rectangular shaped vortices. This analytical model is expected to aid in the effective micromixer design.
[DOI: 10.1115/1.4042469]

Keywords: electro-osmotic flow, stream function, heterogeneously charged surface, zeta potential

1 Introduction

In recent years, lab-on-a-chip microfluidic devices have been used for biochemical detection [1], DNA hybridization [2], drug delivery [3], electrokinetic transport [4], and cell cytometry [5]. These devices generally made up of thin glasses or plastic for concentration [6], sensing [7], and separation [8]. Two basic unit of operations for these devices are pumping [9] and micromixing [10]. Although various pumping mechanisms [11–14] have been reported, very slow mixing of species is a major concern for ultrafast sensing and high throughput separation. Because of the very low Reynolds number ($\mathrm{Re} < 1$) creeping flow in microdevice, mixing of species occurs mostly by diffusion, which is inherently very slow process. Thus, development of an effective micromixer is imperative [14] for fast separation and sensing in lab-on-a-chip microfluidic devices.

Depending on the actuation mechanism, micromixer can be broadly classified into two categories: passive and active. In passive micromixer, the channel geometry is modified to enhance the mixing region by stretching and folding of fluid streams [15,16]. In an experimental work, Wu and Li [17] demonstrated an effective mixing mechanism by using embedded metal hurdle inside a microchannel. Sudarsan and Ugaz [18] designed different microchannels for mixing by altering flow curvature and channel width to generate multivortex based on the Dean flow. Mengeaud et al. [19] demonstrated the mixing effectiveness of zigzag shaped microchannel both experimentally and numerically. Although the working principle of a passive mixer is quite simple, these type of micromixers generally need complex three-dimensional (3D) channel shape, and the resultant pressure drop along the channel is generally much higher than the planar channel configuration.

Active micromixer can circumvent some of the shortcomings of their counterparts. A number of different actuation mechanisms such as acoustic [20], magnetic [21], electrokinetic [22,23] have been reported for active mixing with various degrees of success. Among them, the electrokinetic micromixing is the widely used since the application of localized electric field is much simpler and can be achieved easily in a microfluidic device. In electrokinetic micromixer, an alternating current (AC) or time-periodic electric field is applied to change the flow direction of mixing species/fluids [24]. In a comprehensive study, Song et al. [25] suggested a methodology to enhance the chaotic mixing mechanism by applying low-frequency square wave electric field. Oddy et al. [26] demonstrated a rapid micromixer by taking advantage of electrokinetic instability. The performance of electrokinetic micromixer can be further enhanced by generating surface heterogeneity along the channel. Many researchers deliberately manufactured the channel surface with particular surface charge patterns to enhance mixing in microdevice. For instance, Wei et al. [2] presented an experimental work with nonuniformly charged microchannel surface fabricated from poly (methyl methacrylate) to enhance DNA–DNA hybridization. Biddiss et al. [27] experimentally visualized the effects of surface charge patterning on mixing efficiency of an electrokinetic micromixer. Their results showed that, with heterogeneously charged micromixer, the mixing efficiencies can be improved between 22% and 68% for an applied electric field range of 70∼555 V/cm.

Although numerous studies, both experimentally and numerically, have reported electrokinetic micromixing, very few analytical models exist to study the flow behavior in an electrokinetic micromixer. Dutta and Beskok [28] presented a detailed mathematical analysis for time-periodic electro-osmotic flow in a microfluidic channel and compared their work with the Stokes' second problem. Erickson and Li [29] analyzed AC electro-osmotic flow in 3D rectangular channel using Green functions. Moghadam [30] obtained an exact analytical solution of AC electro-osmotic flow in an annulus microchannel by using Green functions. Although these studies explain the fundamental of electro-osmotic flow, uniform surface potential distribution limits the application of these studies for micromixing. Later, some researchers investigated direct current (DC) electrokinetic flow with heterogeneously

[1]Corresponding author.

Contributed by the Fluids Engineering Division of ASME for publication in the Journal of Fluids Engineering. Manuscript received September 5, 2018; final manuscript received January 2, 2019; published online January 30, 2019. Assoc. Editor: Shizhi Qian.

charged surface. For instance, Anderson and Idol [31] developed an analytical solution for DC electro-osmotic flow with sinusoidal distribution of zeta potential, while Horiuchi et al. [32] presented analytical solution of flow field for sudden changes in zeta potential. In addition, Ng and Chen [33] formulated an analytical solution for steady electro-osmotic flow through a slit microchannel with longitudinal step changes in zeta potential. Chu and Ng [34] analytically studied the steady electro-osmotic flow through a circular tube with variable surface charge conditions. *However, no analytical solution exists for time-periodic electro-osmotic flow with nonuniform zeta potential along the channel*. Nonuniform surface charges along the channel can create vortices, which can enhance mixing of two adjacent streams. In this study, a generic analytical solution is presented for flow field in time-periodic electro-osmotic flow considering arbitrary surface charge distribution along a two-dimensional (2D) straight (planar) microchannel. Two different surface charge distributions are studied to demonstrate the effectiveness of the model.

2 Mathematical Model

Figure 1 illustrates the schematic view of our two-dimensional microchannel, where the surface charges on both upper and lower surfaces can vary in an arbitrary manner. Thus, an electric double layer (EDL) will form in contact with an aqueous solution. An AC electric field (**E**) can be used to generate time-periodic electro-osmotic flow due to the interaction between applied field and EDL. The flow generated by the electric field can be modeled by the continuity and modified Navier–Stokes equations, respectively,

$$\nabla \cdot \mathbf{V} = 0 \tag{1}$$

$$\rho_c \left(\frac{\partial \vec{V}}{\partial t} + \left(\vec{V} \cdot \nabla \right) \vec{V} \right) = -\nabla \mathrm{P} + \mu \nabla^2 \vec{V} + \rho_e \vec{E} \tag{2}$$

where ρ_c is the fluid density, ρ_e is the net charge density, μ is the dynamic viscosity, and P is the pressure. In a typical microfluidic device, the thickness of electrical double layer ranges from 1 to 10 nm and general microchannel height varies from 10 to 100 μm. Therefore, for the purpose of modeling, the bulk liquid flow outside the EDL, the driving force term, $\rho_e \vec{E}$, can be dropped off, and the electro-osmotic effect can be modeled by introducing a slip velocity at the channel wall as

$$u_{\text{wall}} = -\frac{\varepsilon \zeta(x)}{\mu} E_x(t) \tag{3}$$

The aforementioned slip boundary condition follows Helmholtz–Smoluchowski formulation, where ε is the permittivity. Here, it is assumed that both viscosity and permittivity are constant and they are independent of time and space. Though the Helmholtz–Smoluchowski formulation, presented in Eq. (3), is originally developed for steady-state DC electro-osmotic flow, it can be used for low frequency AC (or time periodic) electro-osmotic flow since the charge relaxation frequency ($f_c = (1/2\pi)(\sigma/\varepsilon) \cong 10^6 \sim 10^8$Hz) is much larger for equilibrium distribution of ions in the electric double layer [24]. Moreover, the Helmholtz–Smoluchowski formulation is widely used to model nonuniform electro-osmotic flow in capillaries [35] and microchannels [32,36,37].

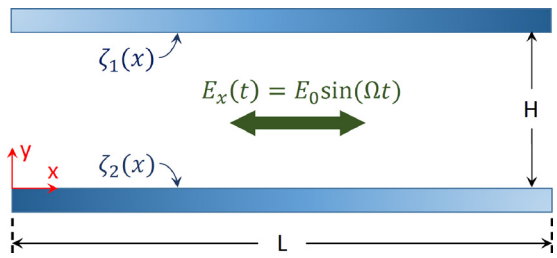

Fig. 1 Schematic of time-periodic electro-osmotic flow with variable surface charge distributions along the channel

For nonuniform surface charge condition, the zeta potentials at the upper and lower surfaces are a function of location along the channel, and they are denoted as $\zeta_1(x)$ and $\zeta_2(x)$, respectively (Fig. 1). In our model problem, the external electric field can be considered as one-dimensional, but it varies with time as

$$E_x(t) = E_{\text{ref}} \sin(\Omega t) = E_0 \sin(\Omega t) \tag{4}$$

where E_0 (E_{ref}) is the reference magnitude of the electric field, and Ω is the angular frequency.

2.1 Assumptions and Approximations. Like any other analytical work, this analysis is based on following assumptions and approximations:

- Liquid inside the channel is considered as an incompressible Newtonian fluid.
- Channel width (W) is sufficiently larger than the channel height (H).
- The advective term is much smaller than the transient and diffusion terms (see the Appendix for justification).
- There is no external pressure gradient along the channel.
- The effect of temperature change is not considered in fluid properties.
- The solvent is continuous, and its permittivity is not affected by local or overall electric field strength.

2.2 Flow Analysis. Based on the aforementioned assumptions, the component form of Naiver–Stokes equations can be presented as

$$\frac{\partial u}{\partial t} = -\frac{1}{\rho_c}\frac{\partial P}{\partial x} + \nu \frac{\partial^2 u}{\partial x^2} + \nu \frac{\partial^2 u}{\partial y^2} \tag{5a}$$

$$\frac{\partial v}{\partial t} = -\frac{1}{\rho_c}\frac{\partial P}{\partial y} + \nu \frac{\partial^2 v}{\partial x^2} + \nu \frac{\partial^2 v}{\partial y^2} \tag{5b}$$

The pressure term from these equations can be dropped by differentiating Eqs. (5*a*) and (5*b*) with respect to y and x, respectively, and then, subtracting one equation from the other. The resultant equation can be written as

$$\frac{\partial \omega}{\partial t} = \nu \nabla^2 \omega \tag{6}$$

where ν is the kinematic viscosity, and ω is the vorticity which is defined as

$$\omega = \frac{\partial u}{\partial y} - \frac{\partial v}{\partial x} \tag{7}$$

The u and v velocities are related to stream function (ψ) as

$$u = \frac{\partial \psi}{\partial y} \quad \text{and} \quad v = -\frac{\partial \psi}{\partial x} \tag{8}$$

respectively. Using the relationship between the velocities and stream function, Eq. (6) can be transformed into a fourth-order partial differential equation

$$\left(-\frac{1}{\vartheta} \left(\frac{\partial}{\partial t} \right) + L^2 \right) L^2 \psi = 0 \tag{9}$$

Table 1 The boundary conditions for models A and B problems

	Model A	Model B
1	$v_{y=0} = -\dfrac{\partial\psi}{\partial x} = 0$	$v_{y=0} = -\dfrac{\partial\psi}{\partial x} = 0$
2	$v_{y=h} = -\dfrac{\partial\psi}{\partial x} = 0$	$v_{y=h} = -\dfrac{\partial\psi}{\partial x} = 0$
3	$u_{y=0} = \dfrac{\partial\psi}{\partial y} = 0$	$u_{y=0} = \dfrac{\partial\psi}{\partial y} = -\dfrac{\varepsilon\zeta_2(x)}{\mu}E_0\exp(i\Omega t)$
4	$u_{y=h} = \dfrac{\partial\psi}{\partial y} = -\dfrac{\varepsilon\zeta_1(x)}{\mu}E_0\exp(i\Omega t)$	$u_{y=h} = \dfrac{\partial\psi}{\partial y} = 0$

where L stands for Laplace operator. Assuming that both externally applied electric field and zeta potential distribution are changing periodically, the target stream function can be described as

$$\psi(x,y,t) = \sum_{n=-\infty}^{\infty} \varphi_n(y)\exp(ik_n x)\exp(i\Omega t) \tag{10}$$

where $k_n = 2\pi n/L$ and n is an integer. Since $-\frac{1}{\vartheta}\left(\frac{\partial}{\partial t}\right) + L^2$ and L^2 are commutative to each other [38], the stream function, $\psi(x,y,t)$ can be linearly decomposed into two parts

$$\psi(x,y,t) = \psi_1(x,y,t) + \psi_2(x,y,t) \tag{11}$$

where

$$\psi_1(x,y,t) = \sum_{n=-\infty}^{\infty} \varphi_{1n}(y)\exp(ik_n x)\exp(i\Omega t) \tag{12}$$

and

$$\psi_2(x,y,t) = \sum_{n=-\infty}^{\infty} \varphi_{2n}(y)\exp(ik_n x)\exp(i\Omega t) \tag{13}$$

Substituting Eqs. (12) and (13) into Eq. (11), one can get the general solutions for $\varphi_{1n}(y)$ and $\varphi_{2n}(y)$ as follows:

$$\varphi_{1n}(y) = C_{1n}e^{k_n y} + C_{2n}e^{-k_n y} \tag{14}$$

$$\varphi_{2n}(y) = C_{3n}e^{k_{1n} y} + C_{4n}e^{-k_{1n} y} \tag{15}$$

where $k_{1n} = \sqrt{k_n^2 + \frac{i\Omega}{\nu}}$. Using Eqs. (11)–(15) and converting exponential terms to hyperbolic functions, the stream function can be presented as a series solution

$$\psi = \sum_{n=-\infty}^{\infty} [D_{1n}\sinh(k_n y) + D_{2n}\cosh(k_n y) + E_{1n}\sinh(k_{1n} y) + E_{2n}\cosh(k_{1n} y)]\exp(ik_n x)\exp(i\Omega t) \tag{16}$$

where D_{1n}, D_{2n}, E_{1n}, and E_{2n} are the coefficients, and their value will depend on the boundary conditions used on the channel surface.

For the problem presented in Fig. 1, we have nonhomogeneous boundary conditions at the upper and lower surface due to zeta potential $\zeta_1(x)$ and $\zeta_2(x)$. Since our governing equation is linear, the system presented in Fig. 1 can be split into two model problems: models A and B (Table 1). Both models have three homogeneous boundary conditions and one nonhomogeneous boundary condition. For model A, the nonhomogenous boundary condition is on the upper wall, while for the model B the nonhomogenous boundary condition is on the lower wall.

2.3 Analytical Solution for the Flow Field. The coefficients of the stream function can be found by using boundary conditions listed in Table 1. For the model A, these four coefficients $(D_{1n}, D_{2n}, E_{1n}, E_{2n},)$ can be conveniently reduced to one (D_{1n}) using boundary conditions 1–3. Thus, the stream function for the model A can be given as

$$\psi_A = \sum_{n=-\infty}^{\infty} D_{1nA}\left[\sinh(k_n y) - \beta_n\cosh(k_n y) - \frac{k_n}{k_{1n}}\sinh(k_{1n} y) + \beta_n\cosh(k_{1n} y)\right]\exp(ik_n x)\exp(i\Omega t) \tag{17}$$

where the eigenvalue (β_n) can be found as

$$\beta_n = \frac{\sinh(k_n h) - \dfrac{k_n}{k_{1n}}\sinh(k_{1n} h)}{\cosh(k_n h) - \cosh(k_{1n} h)} \tag{18}$$

The remaining coefficient (D_{1n}) can be found from the slip boundary condition at the channel wall. Any periodic zeta potential distribution along the channel wall (top) can be expressed as a complex Fourier series using Eq. (19)

$$\zeta_1(x) = \sum_{n=-\infty}^{\infty} C_n\exp(ik_n x) \tag{19}$$

where C_n is the Fourier coefficient, which can be expressed as

$$C_n = \frac{1}{L}\int_0^L \zeta_1(x)\exp(-ik_n x)dx \tag{20}$$

Therefore, the slip boundary condition in Table 1 become

$$u_{\text{wall}} = \frac{\partial\psi}{\partial y} = -\frac{\varepsilon E_0}{\mu}\exp(i\Omega t)\sum_{n=-\infty}^{\infty} C_n\exp(ik_n x) \tag{21}$$

By applying the inhomogeneous boundary condition (Eq. (21)), the last unknown coefficient, D_{1n} for model A becomes

$$D_{1nA} = -\frac{\varepsilon E_0}{\mu}C_n\left[\frac{1}{k_n\cosh(k_n h) - k_n\beta_n\sinh(k_n h) - k_n\cosh(k_{1n} h) + k_{1n}\beta_n\sinh(k_{1n} h)}\right] \tag{22}$$

The velocity components for the model A can be obtained by taking first derivative of the stream function (Eq. (17)) as

$$u_A = \frac{\partial \psi_A}{\partial y} = \mathrm{Im}\left[\sum_{n=-\infty}^{\infty} D_{1nA}\left\{k_n \cosh(k_n y) - \beta_n k_n \sinh(k_n y) - k_n \cosh(k_{1n} y) + \beta_n k_{1n} \sinh(k_{1n} y)\right\} \exp(ik_n x)\exp(i\Omega t)\right] \tag{23}$$

$$v_A = -\frac{\partial \psi_A}{\partial x} = \mathrm{Im}\left[\sum_{n=-\infty}^{\infty} -D_{1nA}\left\{\sinh(k_n y) - \beta_n \cosh(k_n y) - \frac{k_n}{k_{1n}}\sinh(k_{1n} y) + \beta_n \cosh(k_{1n} y)\right\} ik_n \exp(ik_n x)\exp(i\Omega t)\right] \tag{24}$$

Likewise, the stream function for the model B can be obtained as

$$\psi_B(x,y,t) = \sum_{n=-\infty}^{\infty} D_{1nB}\left\{\sinh(k_n y) - \gamma_n \cosh(k_n y) + \tau_n \sinh(k_{1n} y) + \gamma_n \cosh(k_{1n} y)\right\} \exp(ik_n x)\exp(i\Omega t) \tag{25}$$

where

$$D_{1nB} = -\frac{\varepsilon E_0}{\mu} C_n \left\{\frac{1}{\left(k_n - \frac{\sinh(k_n h)}{\sinh(k_{1n} h)} k_{1n} + \frac{\gamma_n \cosh(k_n h)}{\sinh(k_{1n} h)} k_{1n} - \frac{\gamma_n \cosh(k_{1n} h)}{\sinh(k_{1n} h)} k_{1n}\right)}\right\} \tag{26}$$

$$\gamma_n = \frac{k_n \cosh(k_n h) - \frac{k_{1n}\sinh(k_n h)}{\tanh(k_{1n} h)}}{k_n \sinh(k_n h) - k_{1n}\sinh(k_{1n} h) - \frac{k_{1n}\cosh(k_n h)}{\tanh(k_{1n} h)} + \frac{k_{1n}(\cosh(k_{1n} h))}{\tanh(k_{1n} h)}} \tag{27}$$

$$\tau_n = \frac{-\sinh(k_n h) + \gamma_n \cosh(k_n h) - \gamma_n \cosh(k_{1n} h)}{\sinh(k_{1n} h)} \tag{28}$$

Thus, the velocity components for the model B are

$$u_B = \frac{\partial \psi_B}{\partial y} = Im\left[\sum_{n=-\infty}^{\infty} D_{1nB}\left\{k_n \cosh(k_n y) - \gamma_n k_n \sinh(k_n y) + \tau_n k_{1n} \cosh(k_{1n} y) + \gamma_n k_{1n} \sinh(k_{1n} y)\right\} \exp(ik_n x)\exp(i\Omega t)\right] \tag{29}$$

$$v_B = -\frac{\partial \psi_B}{\partial x} = Im\left[\sum_{n=-\infty}^{\infty} -D_{1nB}\left\{\sinh(k_n y) - \gamma_n \cosh(k_n y) + \tau_n \sinh(k_{1n} y) + \gamma_n \cosh(k_{1n} y)\right\} ik_n \exp(ik_n x)\exp(i\Omega t)\right] \tag{30}$$

3 Validation

In order to validate the results of this work, we have compared our solution with published analytical results [39]. Datta and Choudhary [39] investigated the DC electro-osmotic flow with sinusoidal surface potential distribution by introducing the Navier slip boundary condition as, $b\partial u/\partial y + u = 0$, where b is the slip length. The value of empirical parameter b is important for very limited cases [40]. By setting $b = 0$, the results are regenerated from Ref. [39] for no slip velocity boundary conditions at the channel wall and those results are used to validate our analytical model. Figure 2 shows the comparison between our results and published work [39] for u-velocity (streamwise direction) distribution at various axial locations. The results are presented for sinusoidal distribution of zeta potential, $\zeta(x) = \zeta_0 \cos\left(\frac{2\pi}{L}x\right)$ where ζ_0 is the (reference) amplitude of the surface potential. With this surface charge distribution, the Fourier coefficient, C_n for our solution can be determined from Eq. (20). Except for $n = 1$ and $n = -1$, C_n has a zero value. For $n = 1$ and $n = -1$, C_n can be given as

$$C_1 = \frac{\zeta_0}{2}, \quad \text{and} \quad C_{-1} = -\frac{\zeta_0}{2} \tag{31}$$

By substituting these coefficients to Eqs. (23), (24), (29), and (30), the final solutions for velocity components are obtained. As shown in Fig. 2, except very small region near the channel wall, our results are in good agreement with Ref. [39]. Discrepancy at the wall is arisen due to the consideration of no-slip at the wall in their work and slip boundary condition at the wall in our model.

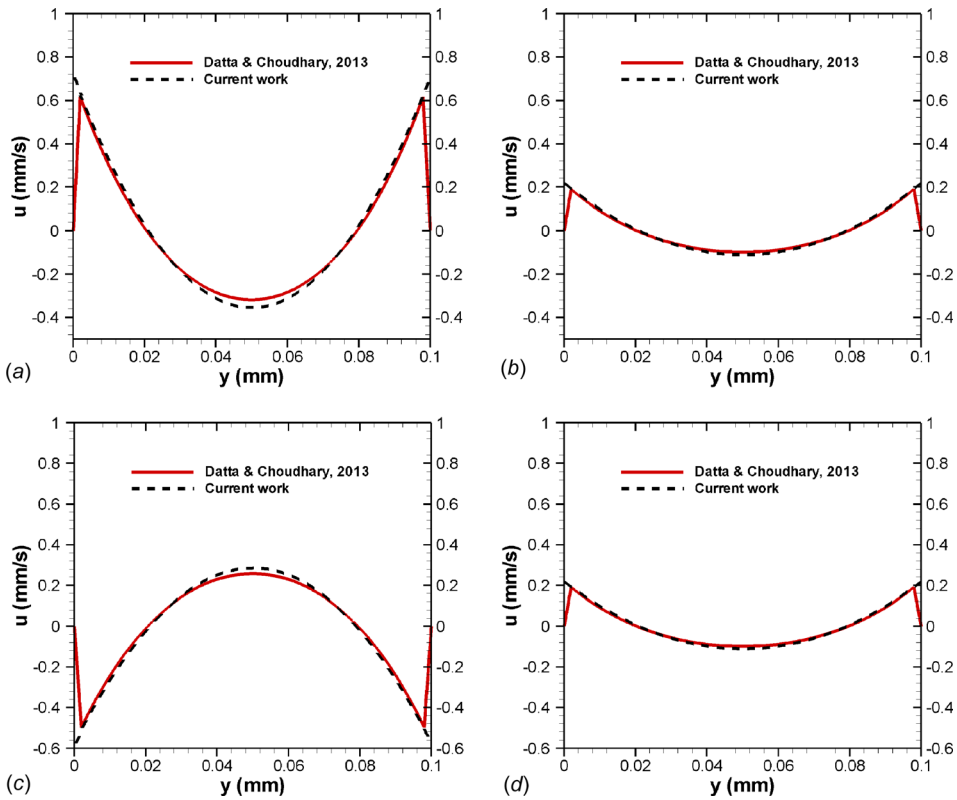

Fig. 2 The *u*-velocity distribution at different axial locations for sinusoidal zeta potential distribution along the channel surface: (*a*) $x = 0$, (*b*) $x = L/5$, (*c*) $x = 3L/5$, and (*d*) $x = 4L/5$. A DC electric field ($E = 10$ KV/m) is used for both studies.

Table 2 Typical length scale, electrokinetic, and flow parameters considered in this theoretical work

Symbols	Parameters	Values
μ	Dynamic viscosity	1×10^{-3} Pa · s
ϑ	Kinetic viscosity	1×10^{-6} m^2/s
σ	Electrolyte conductivity	$2.1 \times 10^{-3} \sim 8.4 \times 10^{-2}$ sm^{-1}
ε_r	Dielectric constant	80
ε_0	Permittivity of free space	8.854×10^{-12} C/Vm
E_{ref} or E_0	Reference electric field	10 kV/m
H	Channel height	50, 100, or 200 μm
f	frequency of electric field	0.1, 1, 10 kHz

4 Results and Discussion

In this section, the applicability of our general solution is demonstrated with different surface charge distribution along the channel wall. Table 2 presents the fluid properties and other parameters used to obtain flow solution from our analytical model. The frequency of electric field is varied from 100 Hz to 10 kHz which is selected based on the works of Green et al. [24] and Chen et al. [41]. Since the frequency of applied electric field is four to six orders of magnitude smaller than the charge relaxation frequency, the use of Eq. (3) is justified to model the electroosmotic effect. The strength of reference electric field is chosen from Herr et al. [42], and channel heights are selected based on Stroock et al. [43]. The buffer solution is same as that used in the experimental work of Green et al. [24]. Although our analytical model is valid for any periodic zeta potential distribution along the length of channel surface, the results are presented only for sinusoidal and step change in zeta potential distributions at both surfaces.

4.1 Sinusoidal Variation of Zeta Potential. For sinusoidal case, the zeta potential distribution along the channel wall can be expressed as $\zeta(x) = \zeta_0 \sin(kx)$, where ζ_0 is the amplitude of the zeta potential. The wave number can be presented as $k = 2\pi/\lambda$, where λ is the wavelength. The value of wavelength depends on the number of periodicity along the channel. For example, $\lambda = L$ corresponds to one complete cycle, whereas, $\lambda = L/2$ represents two complete cycles along the channel. For this particular case, the Fourier coefficient becomes

$$C_n = \frac{\zeta_0}{L}\left[\frac{\{ik_n \sin(kL) + k\cos(kL)\}e^{-ik_nL} - k}{k_n^2 - k^2}\right] \tag{32}$$

4.1.1 Symmetric Zeta Potential Distribution. Figure 3 illustrates the velocity vector at different nondimensional time (Ωt) for sinusoidal zeta potential distribution along the channel at both top and bottom surfaces ($\zeta_{1,2}(x) = \zeta_0 \sin(2\pi/Lx)$). At $\Omega t = \pi/2$, due to positive electric field and negative surface zeta potential in the left half of channel ($x < L/2$), fluids near the top walls move in positive x-direction. However, in contrary, due to positive electric field and positive surface charge in the right half of channel ($x > L/2$), fluids near the top walls move in negative x-direction. These two opposite directional flows create two counter rotating vortices in the upper half of the channel (Fig. 3(*a*)). Due to the same reason, two counter rotating vortices are also formed in the lower half of the channel. However, these two vortices are in opposite phase of upper half vortices due to same surface potential distribution on both surfaces. Therefore, clockwise circulation of fluids occurs in the top-left and bottom-right quarters of the channel and anticlockwise circulation of fluids occurs in the bottom-left and top-right quarters of the channel. Thus, if the channel is filled with two fluids in such a way that each fluid fills full height and one-fourth length of the channel in an alternative patch, this type of vortices can enhance the mixing.

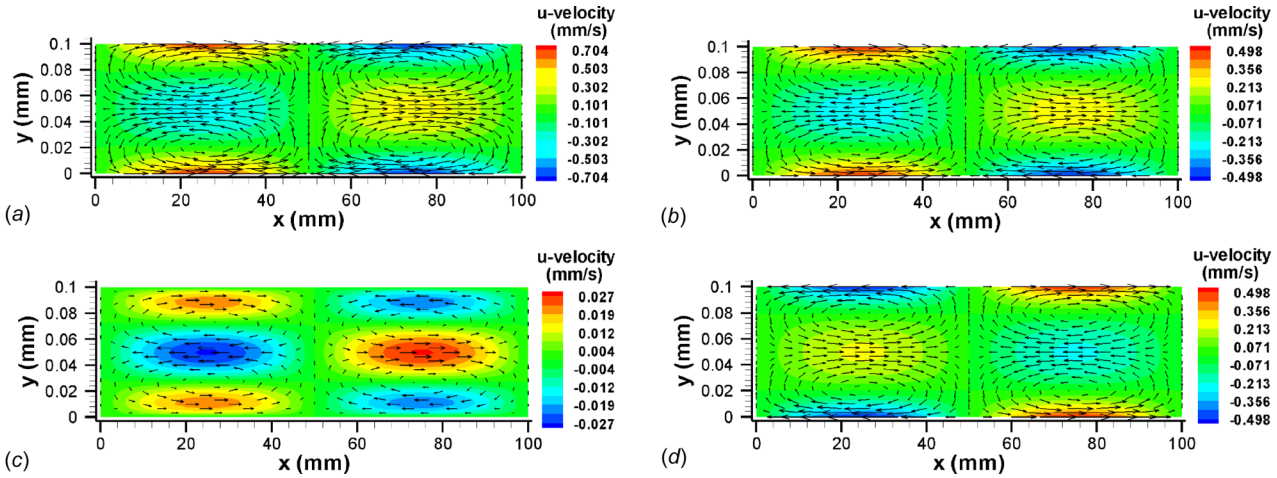

Fig. 3 The velocity vector field and *u*-velocity contours with sinusoidal zeta potential distribution at both top and bottom walls at various nondimensional times: (*a*) $= (\pi/2)$, (*b*) $\Omega t = (3\pi/4)$, (*c*) $\Omega t = \pi$, and (*d*) $\Omega t = (5\pi/4)$. Here $f = 100$ Hz, $k = (2\pi/L)$, $H = 100$ μm, $\zeta_0 = -100$ mV, $E_{ref} = 10$ (*kV/m*).

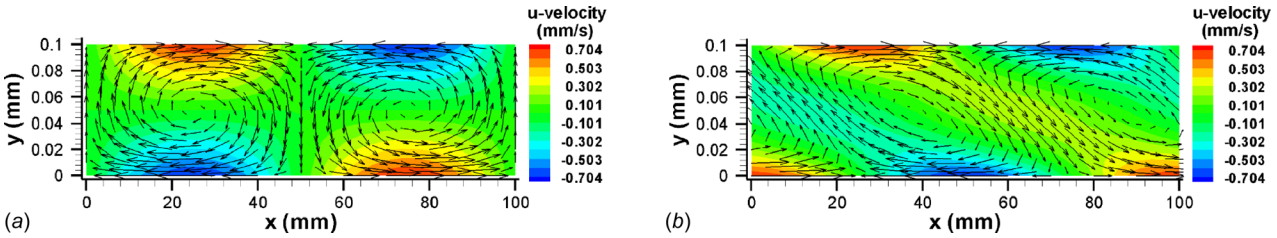

Fig. 4 The velocity vector field and *u*-velocity contours for asymmetric surface potential distribution on upper and lower surfaces: (*a*) upper surface: $\zeta_1(x) = \zeta_0 \sin(kx)$, lower surface: $\zeta_2(x) = -\zeta_0 \sin(kx)$ and (*b*) upper surface: $\zeta_1(x) = \zeta_0 \sin(kx)$, lower surface: $\zeta_2(x) = \zeta_0 \cos(kx)$. Here $f = 100$ *Hz*, $\Omega t = (\pi/2)$, $k = (2\pi/L)$, $H = 100$ μm, $\zeta_0 = -100$ mV, $E_{ref} = 10$ kV/m.

Figure 3(*b*) shows vector plot of flow field at nondimensional time, $\Omega t = 3\pi/4$. This yields similar results as previous case (Fig. 3(*a*)) due to similar conditions, however, the magnitude of velocity components is proportionally reduced with the applied electric field. At normalized time, $\Omega t = \pi$, the slip velocity at the wall reaches to zero due to no applied electric field value (Fig. 3(*c*)). However, a small bulk fluid motion is still observed at the center region of the channel. This small motion is arisen from the phase lag between fluids in the electric double layer and bulk fluid regions due to the finite time requirement for momentum diffusion [29]. This out of phase behavior, as shown in Fig. 3(*c*), is similar to the Stokes oscillating plate problem [44]. When electric field changes it direction, the velocity streamlines also switch its direction (Fig. 3(*d*)). An anticlockwise circulation of fluids occurs in the top-left and bottom-right quarters of the channel, while clockwise circulation of fluids are observed in the bottom-left and top-right quarters of the channel. At any transverse location ($y =$ cons.), $u-$ velocity varies sinusoidally with axial location of the channel. However, at low frequency (<100 Hz), $u-$ velocity at any axial location ($x =$ cons.) varies parabolically along the transverse direction (data are not shown). Unlike pure electro-osmotic flow, plug-like velocity profile cannot be achieved in time periodic electro-osmotic flow.

4.1.2 Asymmetric Surface Zeta Potential Distribution. Next, we present the velocity distribution for asymmetric surface potential distributions along the channel. Figure 4(*a*) shows velocity vector plot for sinusoidal surface potential distribution at walls, where the surface zeta potential has a 180 deg phase difference between upper and lower surfaces. In contrast to symmetric surface zeta potential distribution (Fig. 3), two vortices are formed instead of four vortices (see Fig. 4(*a*)). At normalized time $\pi/2$, fluids near the left-half of top surface flow to positive x-direction due to negative surface zeta potential, whereas, fluids near the right-half of top surface flow to negative x-direction due to positive zeta potential. These two opposite directional flows create a vertically downward motion at the center ($x = L/2$) of the channel. An opposite phenomenon occurs near the bottom surface, due to opposite zeta potential distribution in bottom surface. As a result, two large vortices are generated in the channel.

Figure 4(*b*) shows velocity vector plot for another case of asymmetric surface zeta potential distribution, where a phase difference of 90 deg is considered between the top and bottom surfaces for zeta potential distributions. Interestingly, it creates two skewed elliptical vortices (Fig. 4(*b*)). Near the left-half of the top surface, fluids flow to positive x-direction due to negative surface charge, whereas, near the right-half of the top surface, fluids flow to negative direction due to positive surface charge. As before, these two opposite directional flows create a negative downward motion at the center of the channel. However, near the first and last quarter of bottom surface, fluids move to positive x-direction due to negative zeta potential, whereas, fluids near the middle part of the bottom surface move to negative x-direction due to positive zeta potential in this part of the surface. This type of vortex formation has great potential for microfluidic mixing applications. For instance, if the upper half of channel is filled with one fluid and lower half of the channel is filled with another fluid, this type of vortices can force fluid streams to mix.

4.1.3 Effect of Periodicity in Zeta Potential Distribution. The number of vortices formed either in symmetric or asymmetric case can be increased by increasing the periodicity of the surface zeta potential distribution along the length of the channel. The effect of one fold increase in zeta potential periodicity is shown in

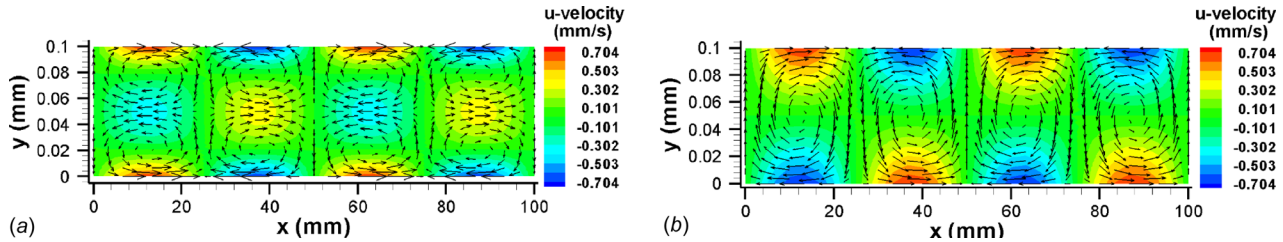

Fig. 5 The effect of periodicity of zeta potential distribution on velocity vector field and *u*-velocity contours: (*a*) upper surface: $\zeta_1(x) = \zeta_0 \sin(kx)$, lower surface: $\zeta_2(x) = \zeta_0 \sin(kx)$ and (*b*) upper surface: $\zeta_1(x) = \zeta_0 \sin(kx)$, lower surface: $\zeta_2(x) = -\zeta_0 \sin(kx)$. Here $f = 100$ Hz, $k = (4\pi/L)$, $\Omega t = (\pi/2)$, $H = 100$ μm, $\zeta_0 = -100$ mV and $E_{ref} = 10$ kV/m.

Fig. 5 for both symmetric and asymmetric cases. Our analytical results reveal that number of vortices can be doubled (from four to eight in symmetric case and from two to four in asymmetric case) in both symmetric and asymmetric cases by doubling the zeta potential periodicity. Further increase in the periodicity will result in proportional increase in number of vorticities in the microchannel. Thus, we can anticipate that by modifying the zeta potential patterning along the channel surface, the flow field can be precisely controlled.

4.1.4 Effect of Frequency of the External Electric Field. The velocity vector fields are shown in Fig. 6 for symmetric zeta potential distribution along the channel surface at different electric field frequencies. Since single period is considered in zeta potential distribution, four vortices are observed within the channel for any electric field frequency. However, as frequency of external electric field increases, the pattern of the flow field changes significantly. For instance, at low electric field frequency (e.g., 100 Hz as shown in Fig. 6(*a*)), each vortex takes possession of one-quarter of the channel. This is because of the fact that at low electric field frequency, the flow gets enough time to propagate from surface to the center of the channel. However, as electric field frequency increases from 100 Hz to 1 kHz, these vortices are slightly shifted toward surfaces and velocity of bulk fluids diminish slightly (Fig. 6(*b*)). When electric field frequency increases from 1 kHz to 10 kHz, the vortices are absolutely confined near the surface and bulk fluid motion reduces significantly, as shown in Fig. 6(*c*). At very high electric field frequency, (10 kHz or higher), the bulk fluids are virtually motionless, even though very fast oscillating flow occurring near the channel surface. A logical explanation for this phenomenon is that as the electric field frequency goes very high, the flow cannot diffuse as fast to develop a flow across the entire channel. More insight into the observed scenario can be dugout by bringing in the frequency-dependent Stokes penetration depth, δ. The Stokes penetration depth is related to frequency and viscosity as

$$\delta \propto \left(\frac{\nu}{\Omega}\right)^{0.5} \tag{33}$$

This length scale is used to describe the oscillatory laminar viscous flows in response to harmonic excitation [44]. Stokes penetration depth shows that the perturbed flow region is inversely proportional to the square root of the frequency. For that reason, the vortices shift toward the channel surface as the electric field frequency increases.

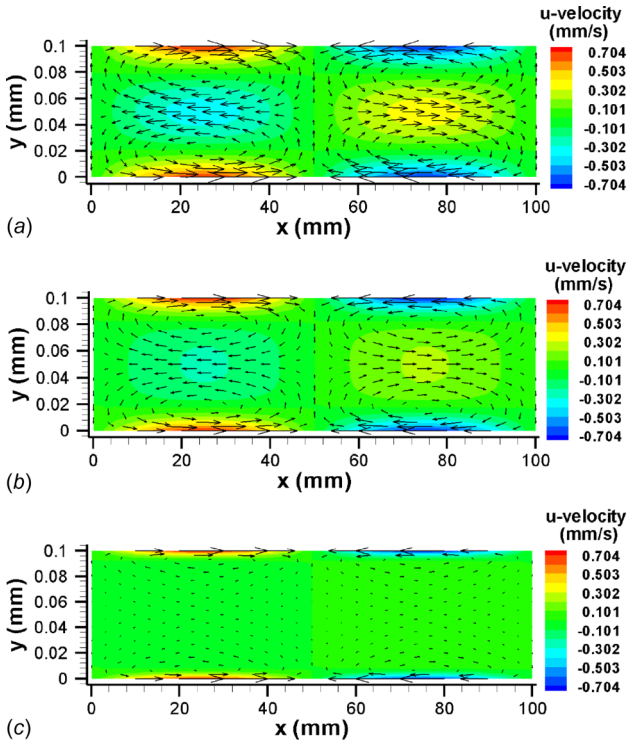

Fig. 6 The effect of external electric field frequency on velocity vector field and *u*-velocity contours for symmetric surface potential distribution: (*a*) $f = 100$Hz, (*b*) $f = 1$kHz, and (*c*) $f = 10$kHz. Here $k = (2\pi/L)$, $\Omega t = (\pi/2)$, $H = 100\mu$m, $\zeta_0 = -100$mV, $E_{ref} = 10$ kV/m.

4.1.5 Effect of Channel Height. The effect of change of channel heights on velocity field is illustrated in Fig. 7. With an increase in channel height from 50 μm to 200 μm, the vortices shift position from center region to near the channel surface (Figs. 7(*a*) and 7(*c*)). In addition to the shift in vortices' position, the motion of bulk fluid is gradually diminished with increasing channel heights. The effect of channel height on flow field is analogous to the effect of electric field frequency. Due to this similarity, several previous studies [29,45], on time-periodic electro-osmotic flow, discussed the effect of these parameters by defining a nondimensional frequency as $\Omega^* = D_h^2/\nu\Omega$, where D_h is the hydraulic diameter. This nondimensional frequency represents the ratio of the diffusion time scale $\left(t_{\text{diff}} = D_h^2/\nu\right)$ and to the period of the applied electric field $(t_{PE} = 1/\Omega)$. For a planar microchannel, the hydraulic diameter is equal to double of the channel height, H. Thus, an increase in channel height results in an increase in diffusion time scale. This higher diffusion time scale indicates that the flow needs more time to develop throughout the channel. Due to this reason, as the channel height increases, the perturbed flow region become smaller and vortices move closer to the channel surface.

4.2 Step Change in Surface Zeta Potential. In Sec. 4.1, we have investigated the electro-osmotic flow through a 2D planar microchannel with sinusoidal surface charge distribution. Although it produces various favorable cases for efficient mixing, fabrication of a microchannel with sinusoidal surface charge distribution is not feasible with current technology. Literature review

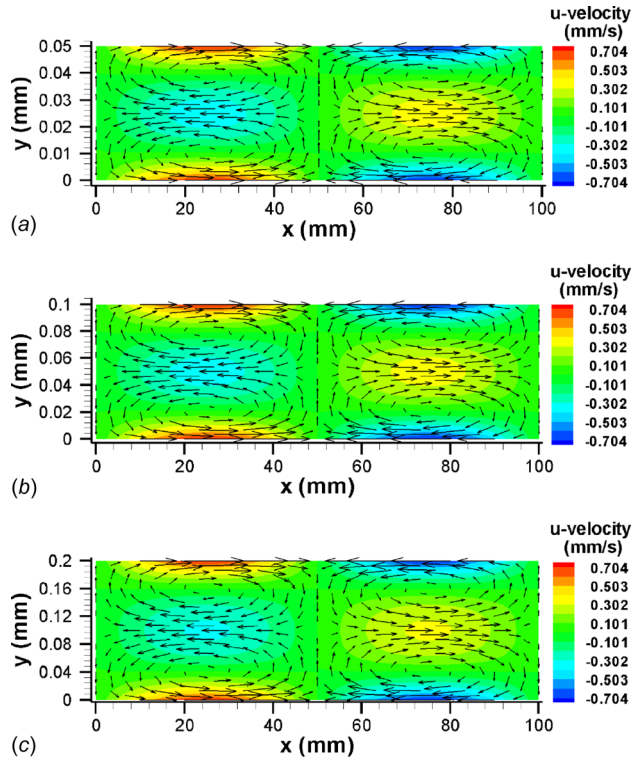

Fig. 7 The effect of channel height on velocity vector field and *u*-velocity contours for symmetric sinusoidal zeta potential distribution: (*a*) $H = 50\mu$m, (*b*) $H = 100\mu$m, and (*c*) $H = 200\mu$m. Here, $f = 100$Hz, $k = (2\pi/L)$, $\Omega t = (\pi/2)$, $\zeta_0 = -100$mV, $E_{ref} = 10$kV/m.

yields that many researchers have investigated, either experimentally or numerically, the electro-osmotic flow with a step change in zeta potential distribution [32]. The results of those studies revealed that this sudden change of surface potential has a lot of potential for efficient mixing within the microchannel. *However, there is no analytical model to investigate the time-periodic electro-osmotic flow through a microchannel with step change in surface potential*. In this section, we applied our generalized analytical model to investigate the time-periodic electro-osmotic flow with step change in surface charge. First, we consider that both top and bottom surfaces have same potential distribution as (Fig. 8)

$$\zeta(x) = \begin{cases} \zeta_1 \left(0 < x < \dfrac{L}{2}\right) \\ -\zeta_1 \left(\dfrac{L}{2} < x < L\right) \end{cases} \tag{34}$$

By expressing this step function in Fourier series (Eq. (19)) as square wave with wavelength L, the coefficient C_n can be given as

$$C_n = \frac{1}{L}\int_0^{\frac{L}{2}} -\zeta_1 \exp(-ik_n x)dx + \frac{1}{L}\int_{\frac{L}{2}}^{L} \zeta_1 \exp(-ik_n x)\,dx \tag{35}$$

This yield $C_n = 0$, if $n = 0$ or n is an even integer. For an odd value of n, the coefficient, C_n can be given as

$$C_n = \frac{2\zeta_1 i}{n\pi} \tag{36}$$

The velocity vector fields for time-periodic electro-osmotic flow through a parallel plate microchannel with symmetric surface

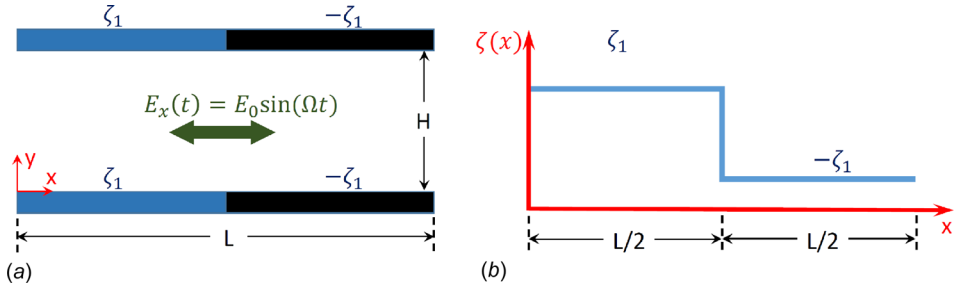

Fig. 8 Schematic of step change in zeta potential along the channel

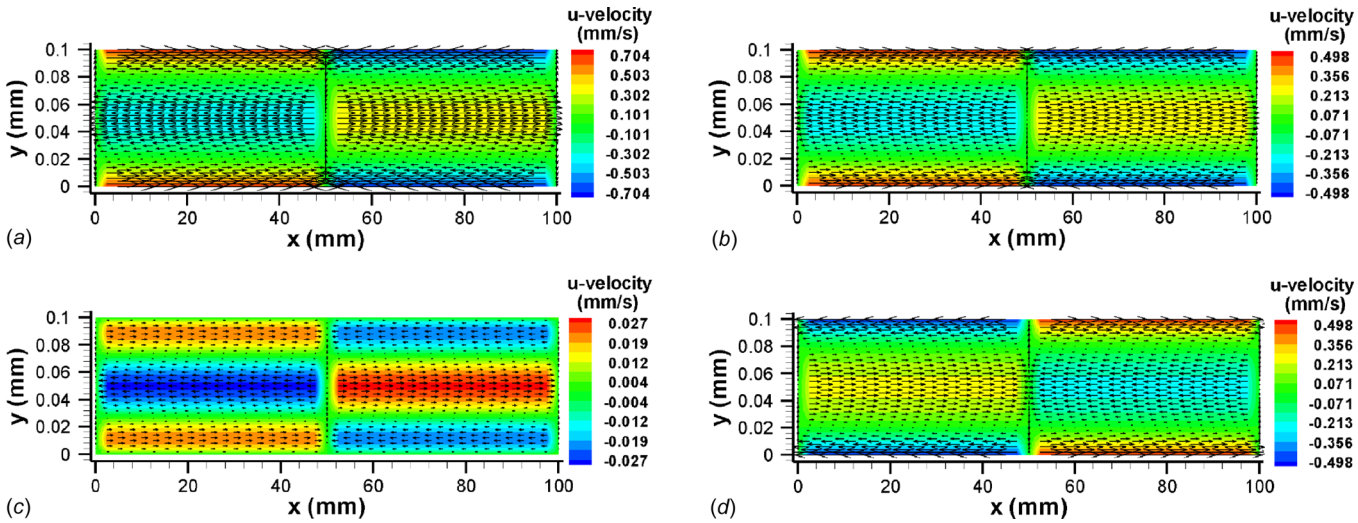

Fig. 9 The velocity vector field and *u*-velocity contours for step change in zeta potential at various nondimensional time: (*a*) $\Omega t = (\pi/2)$, (*b*) $\Omega t = (3\pi/4)$, (*c*) $\Omega t = \pi$ and (*d*)$\Omega t = (5\pi/4)$. Here $f = 100$Hz, $k = (2\pi/L)$, $H = 100\mu$m, $\zeta_1 = -100$mV, $E_{ref} = 10$kV/m.

zeta potential are presented in Fig. 9. Like sinusoidal distribution of surface charge, four vortices are formed with wavelength L at nondimensional time, $\Omega t = \pi/2$. However, in case of step change, the shape of the vortices is not same as vortices formed in sinusoidal case. Instead of elliptical vortices, rectangular shape vortices are formed for step change in zeta potential case because the v-velocity component is almost zero except at the start ($x = 0$), end ($x = L$), and mid-section ($x = L/2$) of the channel where transition in zeta potential and u-velocity take place. Like, sinusoidal zeta potential distribution case (Figs. 3(*a*) and 3(*b*)), intensity of velocity field is slightly diminished due to smaller value of electric field as nondimensional time changes from $\pi/2$ to $3\pi/4$. When the value of nondimensional time becomes zero or π, velocity of fluids near the surface becomes zero (Fig. 9(*c*)). However, like sinusoidal case described before, small motion is observed at the bulk area because of phase lag between the near surface and bulk fluid regions. Finally, at $\Omega t = 5\pi/4$, the overall flow direction reverses in accordance with the change of direction of external electric field (Fig. 9(*d*)).

Similar to sinusoidal surface charge distribution, flow fields for step changes in charge distribution are analyzed for relevant parameters such as wavenumber, electric field frequency, channel heights, and asymmetric charge distribution. However, for brevity, we have not presented them in details. In brief, larger wavenumber generates higher number of vortices. For example, if periodicity is doubled within the length L, the number of vortices is also doubled for both symmetric and asymmetric distribution of step change in zeta potential. Like sinusoidal zeta potential case, symmetric surface potential produces double number of vortices than asymmetric case. In asymmetric cases, vortices are larger and probably have more mixing potential than symmetric zeta potential distribution. Electric field frequency and channel heights also have similar effect like sinusoidal zeta potential distribution. As the channel height or electric field frequency increases, the vortices shift toward the channel surface. At higher normalized frequency, the perturbed flow region becomes smaller and the bulk fluid motion diminishes.

5 Summary and Conclusions

A generalized analytical solution is presented for time-periodic electro-osmotic flow through a 2D microchannel considering arbitrary potential distribution along the channel. The analytical solution is validated by reproducing some published works for DC electro-osmotic flow with sinusoidal zeta potential distribution. The applicability of the developed analytical model was tested for different surface potential distribution, such as sinusoidal and step change. Our results show that surface heterogeneity combined with altering electric field not only generates periodic flow motion but also develops several counter-rotating vortices inside microchannel. Sinusoidal charge distribution produces stronger vortices than step change in surface potential. In summary, from this analytical work, the following conclusions can be drawn:

(1) The number of vortices formed inside the microchannel will depend on the wavelength, i.e., the wave number of surface potential distribution.
(2) The shape of the developed vortices is mainly determined by the patterns of surface charge. For instance, sinusoidal surface charge distribution produces elliptical vortices, whereas step change in surface charge distribution produces rectangular vortices.
(3) For the same wavenumber, symmetric surface electric potential distribution (same distribution in both top and bottom surface) creates double number of vortices than asymmetric case (different surface potential distribution in each plate). Asymmetric case vortices are larger in size, stronger in strength, and probably more useful from practical point of view than symmetric cases.
(4) Both electric field frequency and channel heights have similar effects on the flow pattern. As their value increases, the vortices migrate toward the channel surface, and the bulk fluid motion starts to decrease. Our results reveal that a smaller value of these parameters will help to enhance the mixing.

Appendix: Dimensionless Momentum Equation

By ignoring the electrokinetic body force term, the nondimensional form of momentum equations can be given as

$$\mathrm{St}\frac{\partial \vec{V}^*}{\partial t^*} + \left(\vec{V}^* \cdot \vec{\nabla}^*\right)\vec{V}^* = -\mathrm{Eu}\vec{\nabla}^* P^* + \left(\frac{1}{\mathrm{Re}}\right)\vec{\nabla}^{*2}\vec{V}^* \quad \text{(A1)}$$

where $\mathrm{St} = (fH/V)$ is the Strouhal number, $\mathrm{Eu} = \left(P_0 - P_\infty/\rho V^2\right)$ is the Euler number, and $\mathrm{Re} = (\rho V H/\mu)$ is the Reynolds number. If we consider the characteristic length (channel height) is 100 μm, reference zeta potential is -100 mV and electric field frequency is 100 Hz, the characteristic electro-osmotic slip velocity will be approximately 0.7 mm/s. For water as a working fluid, the corresponding flow Reynolds number is 0.07 and the Strouhal number (St) is 14. Consequently, the convective term can be negligible compared to the transient and diffusion terms (see Table 3).

Table 3 Dimensionless parameter for different frequency and channel height

Frequency (Hz)	Channel height (μm)	Re	St
100	50	0.035	7.14
	100	0.07	14.28
	200	0.14	28.6
1000	50	0.035	71.4
	100	0.07	142.8
	200	0.14	286

References

[1] Choi, J. W., Oh, K. W., Thomas, J. H., Heineman, W. R., Halsall, H. B., Nevin, J. H., Helmicki, A. J., Henderson, H. T., and Ahn, C. H., 2002, "An Integrated Microfluidic Biochemical Detection System for Protein Analysis With Magnetic Bead-Based Sampling Capabilities," Lab Chip, **2**(1), pp. 27–30.
[2] Wei, C. W., Young, T. H., and Cheng, J. Y., 2005, "Electroosmotic Mixing Induced by Non-Uniform Zeta Potential and Application for DNA Microarray in Microfluidic Channel," Biomed. Eng.: Appl., Basis Commun., **17**(6), pp. 281–283.
[3] Dittrich, P. S., and Manz, A., 2006, "Lab-on-a-Chip: Microfluidics in Drug Discovery," Nat. Rev. Drug Discovery, **5**(3), pp. 210–218.
[4] Nandigana, V. V. R., and Aluru, N. R., 2013, "Nonlinear Electrokinetic Transport Under Combined AC and DC Fields in Micro/Nanofluidic Interface Devices," ASME J. Fluids Eng., **135**(2), p. 021201.
[5] Huh, D., Gu, W., Kamotani, Y., Grotberg, J. B., and Takayama, S., 2005, "Microfluidics for Flow Cytometric Analysis of Cells and Particles," Physiol. Meas., **26**(3), pp. R73–R98.
[6] Bhatt, K. H., Grego, S., and Velev, O. D., 2005, "An AC Electrokinetic Technique for Collection and Concentration of Particles and Cells on Patterned Electrodes," Langmuir, **21**(14), pp. 6603–6612.
[7] Perozziello, G., 2017, "Nanoplasmonic and Microfluidic Devices for Biological Sensing," *Nano-Optics: Principles Enabling Basic Research and Applications. NATO Science for Peace and Security Series B: Physics and Biophysics*, B. Di Bartolo, J Collins, and L. Silvestri, eds., Springer, Dordrecht, The Netherlands, pp. 247–274.
[8] Sajeesh, P., and Sen, A. K., 2014, "Particle Separation and Sorting in Microfluidic Devices: A Review," Microfluid. Nanofluid., **17**(1), pp. 1–52.
[9] Hossan, M. R., Dutta, D., Islam, N., and Dutta, P., 2018, "Review: Electric Field Driven Pumping in Microfluidic Device," Electrophoresis, **39**(5–6), pp. 702–731.
[10] Capretto, L., Cheng, W., Hill, M., and Zhang, X., 2011, "Micromixing Within Microfluidic Devices," *Microfluidics. Topics in Current Chemistry*, Vol. 304, B. Lin, ed., Springer, Berlin, pp. 27–68.
[11] Chen, C. H., and Santiago, J. G., 2002, "A Planar Electroosmotic Micropump," J. Microelectromech. Syst., **11**(6), pp. 672–683.

[12] Lemoff, A. V., and Lee, A. P., 2000, "An AC Magnetohydrodynamic Micropump," Sens. Actuators B, **63**(3), pp. 178–185.
[13] Wang, P., Chen, Z. L., and Chang, H. C., 2006, "A New Electro-Osmotic Pump Based on Silica Monoliths," Sens. Actuators B, **113**(1), pp. 500–509.
[14] Vanlintel, H. T. G., Vandepol, F. C. M., and Bouwstra, S., 1988, "A Piezoelectric Micropump Based on Micromachining of Silicon," Sens. Actuators, **15**(2), pp. 153–167.
[15] Gobby, D., Angeli, P., and Gavriilidis, A., 2001, "Mixing Characteristics of T-Type Microfluidic Mixers," J. Micromech. Microeng., **11**(2), pp. 126–132.
[16] Lin, C. H., Fu, L. M., and Chien, Y. S., 2004, "Microfluidic T-Form Mixer Utilizing Switching Electroosmotic Flow," Anal. Chem., **76**(18), pp. 5265–5272.
[17] Wu, Z. M., and Li, D. Q., 2008, "Micromixing Using Induced-Charge Electrokinetic Flow," Electrochim. Acta, **53**(19), pp. 5827–5835.
[18] Sudarsan, A. P., and Ugaz, V. M., 2006, "Multivortex Micromixing," Proc. Natl. Acad. Sci. U. S. A., **103**(19), pp. 7228–7233.
[19] Mengeaud, V., Josserand, J., and Girault, H. H., 2002, "Mixing Processes in a Zigzag Microchannel: Finite Element Simulations and Optical Study," Anal. Chem., **74**(16), pp. 4279–4286.
[20] Liu, R. H., Yang, J. N., Pindera, M. Z., Athavale, M., and Grodzinski, P., 2002, "Bubble-Induced Acoustic Micromixing," Lab Chip, **2**(3), pp. 151–157.
[21] Lu, L. H., Ryu, K. S., and Liu, C., 2002, "A Magnetic Microstirrer and Array for Microfluidic Mixing," J. Microelectromech. Syst., **11**(5), pp. 462–469.
[22] Chang, C. C., and Yang, R. J., 2007, "Electrokinetic Mixing in Microfluidic Systems," Microfluid. Nanofluid., **3**(5), pp. 501–525.
[23] Wang, Y., Zhe, J., Dutta, P., and Chung, B. T., 2007, "A Microfluidic Mixer Utilizing Electrokinetic Relay Switching and Asymmetric Flow Geometries," ASME J. Fluids Eng., **129**(4), pp. 395–403.
[24] Green, N. G., Ramos, A., Gonzalez, A., Morgan, H., and Castellanos, A., 2000, "Fluid Flow Induced by Nonuniform AC Electric Fields in Electrolytes on Microelectrodes—I: Experimental Measurements," Phys. Rev. E, **61**(4), pp. 4011–4018.
[25] Song, H. J., Cai, Z. L., Noh, H., and Bennett, D. J., 2010, "Chaotic Mixing in Microchannels Via Low Frequency Switching Transverse Electroosmotic Flow Generated on Integrated Microelectrodes," Lab Chip, **10**(6), pp. 734–740.
[26] Oddy, M. H., Santiago, J. G., and Mikkelsen, J. C., 2001, "Electrokinetic Instability Micromixing," Anal. Chem., **73**(24), pp. 5822–5832.
[27] Biddiss, E., Erickson, D., and Li, D. Q., 2004, "Heterogeneous Surface Charge Enhanced Micromixing for Electrokinetic Flows," Anal. Chem., **76**(11), pp. 3208–3213.
[28] Dutta, P., and Beskok, A., 2001, "Analytical Solution of Time Periodic Electroosmotic Flows: Analogies to Stokes' Second Problem," Anal. Chem., **73**(21), pp. 5097–5102.
[29] Erickson, D., and Li, D. Q., 2003, "Analysis of Alternating Current Electroosmotic Flows in a Rectangular Microchannel," Langmuir, **19**(13), pp. 5421–5430.
[30] Moghadam, A. J., 2013, "Exact Solution of AC Electro-Osmotic Flow in a Microannulus," ASME J. Fluids Eng., **135**(9), p. 091201.
[31] Anderson, J. L., and Keith Idol, W., 1985, "Electroosmosis Through Pores With Nonuniformly Charged Walls," Chem. Eng. Commun., **38**(3–6), pp. 93–106.
[32] Horiuchi, K., Dutta, P., and Ivory, C. F., 2007, "Electroosmosis With Step Changes in Zeta Potential in Microchannels," AIChE J., **53**(10), pp. 2521–2533.
[33] Ng, C. O., and Chen, B., 2013, "Dispersion in Electro-Osmotic Flow Through a Slit Channel With Axial Step Changes of Zeta Potential," ASME J. Fluids Eng., **135**(10), p. 101203.
[34] Chu, H. C. W., and Ng, C. O., 2012, "Electroosmotic Flow Through a Circular Tube With Slip-Stick Striped Wall," ASME J. Fluids Eng., **134**(11), p. 111201.
[35] Potoček, B., Gaš, B., Kenndler, E., and Štědrý, M., 1995, "Electroosmosis in Capillary Zone Electrophoresis With Non-Uniform Zeta Potential," J. Chromatogr. A, **709**(1), pp. 51–62.
[36] Lee, J. S. H., Ren, C. L., and Li, D. Q., 2005, "Effects of Surface Heterogeneity on Flow Circulation in Electroosmotic Flow in Microchannels," Anal. Chim. Acta, **530**(2), pp. 273–282.
[37] Chang, C. C., and Yang, R. J., 2006, "A Particle Tracking Method for Analyzing Chaotic Electroosmotic Flow Mixing in 3D Microchannels With Patterned Charged Surfaces," J. Micromech. Microeng., **16**(8), pp. 1453–1462.
[38] Tomotika, S., 1935, "On the Instability of a Cylindrical Thread of a Viscous Liquid Surrounded by Another Viscous Fluid," Proc. R. Soc. Lond. A, **150**(870), pp. 322–337.
[39] Datta, S., and Choudhary, J. N., 2013, "Effect of Hydrodynamic Slippage on Electro-Osmotic Flow in Zeta Potential Patterned Nanochannels," Fluid Dyn. Res., **45**(5), p. 055502.
[40] Schonecker, C., Baier, T., and Hardt, S., 2014, "Influence of the Enclosed Fluid on the Flow Over a Microstructured Surface in the Cassie State," J. Fluid Mech., **740**, pp. 168–195.
[41] Chen, J. K., Weng, C. N., and Yang, R. J., 2009, "Assessment of Three AC Electroosmotic Flow Protocols for Mixing in Microfluidic Channel," Lab Chip, **9**(9), pp. 1267–1273.
[42] Herr, A. E., Molho, J. I., Santiago, J. G., Mungal, M. G., Kenny, T. W., and Garguilo, M. G., 2000, "Electroosmotic Capillary Flow With Nonuniform Zeta Potential," Anal. Chem., **72**(5), pp. 1053–1057.
[43] Stroock, A. D., Dertinger, S. K. W., Ajdari, A., Mezic, I., Stone, H. A., and Whitesides, G. M., 2002, "Chaotic Mixer for Microchannels," Science, **295**(5555), pp. 647–651.
[44] Panton, R. L., 2006, *Incompressible Flow*, 3rd ed., Wiley, New York, Chap. 11.
[45] Moghadam, A. J., 2012, "An Exact Solution of AC Electro-Kinetic-Driven Flow in a Circular Micro-Channel," Eur. J. Mech. B Fluids, **34**, pp. 91–96.